Journal of Zhejiang University-SCIENCE A in press
www.jzus.zju.edu.cn; www.springer.com/journal/11582
E-mail: jzus_a@zju.edu.cn

Research Article

https://doi.org/10.1631/jzus.A2500501

A wear map-based wear prediction method for the piston/cylinder interface in axial piston machines

Fei LYU[1,2], Xudong SHEN[1], Felix SCHLEGEL[2], Xiaolong ZHANG[1] ✉, Liangyu SONG[1], Junhui ZHANG[1], Katharina SCHMITZ[2], Bing XU[1]

[1]State Key Laboratory of Fluid Power and Mechatronic Systems, Zhejiang University, Hangzhou 310058, China
[2]Institute for Fluid Power Drives and Systems (ifas), RWTH Aachen University, Aachen 52074, Germany

Abstract: Understanding the wear behavior of the piston/cylinder interface (PCI) is critical for improving the reliability and service life of axial piston machines (APMs). Existing PCI wear prediction methods often rely on one or two predefined wear models, for example the Archard model, with simplified mechanism switching. However, the PCI inherently experiences multiple coexisting contact states. In this paper, we propose a wear map-based wear prediction method. The operating conditions that can comprehensively represent the contact states across the entire interface are simulated by a mixed lubrication model and are then used as a matrix input into tribometer tests to measure a map of the wear rate. The wear map establishes the quantitative correlations between the contact states and the wear rate and can be embedded into an existing PCI wear prediction framework. An APM wear test showed that our proposed method could track the wear evolution process and capture the wear redistribution in the end region of the cylinder bore under the investigated operating conditions.

Key words: Wear map; Wear evolution; Mixed lubrication; Piston/cylinder interface; Axial piston machine

1 Introduction

Axial piston machines (APMs) serve as the core hydraulic power source of hydraulic transmission systems and are widely used in heavy production lines, mobile machines, and aircraft flight control systems. Fig. 1 shows a structural schematic of a swash plate type APM. The working principle of an APM involves the reciprocating motion of pistons within their respective chambers, which changes the chamber volume to achieve oil suction and discharge. The piston/cylinder interface (PCI) is one of the most significant lubricating interfaces and maintains the functions of lubricating, load bearing, and sealing of the APM. The PCI operates under a large lateral force without static pressure support. The risk of wear failure is high, and the consequences are serious. Clarifying the law of the wear process is a feasible way to prevent a sudden wear failure (Xia et al., 2022; Kumar, 2024).

The contact states across the entire PCI are extremely uneven due to complicated component dynamics and alternating pressure boundaries, leading to an uneven wear topography that in turn affects contact states. The coupled evolution between the wear topography and contact states makes it challenging to simulate the wear process of the PCI. A simulation framework to address this issue has been proposed recently (Lyu et al., 2020). The mainstream approach involves calculating parameters such as the solid contact stress and the film thickness ratio through developed mixed lubrication models, followed by selecting the corresponding wear model to calculate the wear volume or roughness degradation. After surface wear occurs, the micron-scale wear topography is considered to re-express the oil film thickness in the Reynolds equation for the PCI. Additionally, the impact of the roughness degradation on lubrication is introduced

---

✉ Xiaolong ZHANG, zhang.xl@zju.edu.cn
Xiaolong ZHANG, https://orcid.org/0000-0003-3368-1212

Received Oct. 10, 2025; Revision accepted Feb. 28, 2026; Crosschecked

through the average flow Reynolds equation (Patir and Cheng, 1978; Lyu et al., 2023). Through this simulation framework, the real-time interaction between interface lubrication and the surface wear topography can be analyzed over time. The prerequisites of precise wear prediction are obtaining accurate contact states and selecting appropriate wear mechanisms for each contact region.

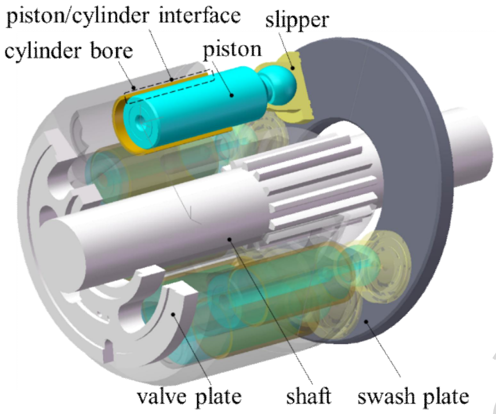

Fig. 1 Schematic diagram of an APM

The contact and lubrication of the PCI have been systematically investigated over recent decades, including tribo-dynamic modeling (Xu et al., 2013; Gärtner et al., 2019; Ransegnola et al., 2022), solutions for thermal-fluid-structure interaction (Ernst and Vacca, 2021; Yin et al., 2023; Zhang et al., 2023; Zhang et al., 2024; Wang et al., 2025) and surface contact modeling with asperity scale resolution (Schenk, 2014; Wondergem and Ivantysynova, 2015; Lyu et al., 2023). These studies have significantly advanced PCI contact and lubrication state prediction. However, in most wear prediction studies the wear calculation step is still dominated by simplified assumptions on wear mechanisms and laws. The research on the wear mechanisms at the PCI has not been as thorough as that on lubrication, and the fundamental mechanisms themselves remain underemphasized.

Brinkschulte et al. (2018) calculated the solid contact stress using a lubrication model of the PCI. The Archard model (Archard, 1953; Lin et al., 2024) was used to calculate the wear of the solid contact regions at the PCI, and an energetic wear model, the Fleischer model (Fleischer, 1973), was used for the non-contact regions. Ivantysyn et al. (2020) and Long et al. (2024) proposed similar models to identify the wear mechanisms according to the contact state of the slipper/swash plate interface, which is another key lubricating interface in APMs. Lyu et al. (2020) analyzed the solid contact stress and film thickness ratio, and used them as criteria to classify the wear mechanisms at the PCI as adhesive wear or two-body abrasive wear (Wen and Huang, 2017; Zhang et al., 2021). From the perspective of wear calculation, these approaches can be summarized as being extremely simplified hard-switching strategies, in which the wear mechanism and the corresponding wear calculation method are switched once a prescribed contact-state criterion is reached. Such hard-switching or single-mechanism modeling is practical, but becomes increasingly restrictive for the PCI, because the complex kinematics and dynamics lead to wide ranges of sliding speed and contact stress and multiple coexisting contact states across the interface. Under these conditions, wear mechanisms cannot be sufficiently explained by simplistic hypotheses of a single mechanism or multiple mechanisms used in previous research.

To address this challenge, in this paper we propose a novel approach that involves determining the contact states across discrete regions of the PCI and conducting corresponding tribological tests to establish the correlation between wear rates and distributed contact states. This correlation can be presented in the form of a wear map, which proves particularly effective for such analysis (Gong et al., 2015; Guo et al., 2019; Mattei et al., 2020; Zhang et al., 2021; Vásquez-Chacón et al., 2022). The contact states, which are characterized by sliding speeds and contact stresses, serve as independent variables in the wear map. After embedding the wear map into the wear prediction framework, the wear rates for each region across the entire interface can be obtained directly, eliminating the risk of misidentifying wear mechanisms and inaccurately calculating wear rates. Compared with the conventional hard-switching methods, the measured wear map provides a more flexible mapping from the contact state, characterized by contact stress and sliding speed, to the wear rate over the operating envelope of the PCI, which is particularly suitable for interfaces with multiple coexisting contact states.

A flow chart of the existing wear prediction framework is explained in Section 2, and the role of the wear map proposed in this framework is indicated. In Section 3, the contact states across the entire interface are described using a lubrication model for the PCI and serve as the operating condition matrix for the following tribometer tests. In Section 4, the wear map is obtained by tribometer tests, and its development is discussed and compared to the most widely used Archard model-based method. Then the wear map is embedded into the PCI wear prediction framework. In Section 5, the effects of the wear map on the wear distribution and the evolution process are analyzed and validated through an APM wear test. In Section 6, conclusions, limitations and the future outlook are discussed.

2 Methodology

An overall flow chart of PCI wear prediction is shown in Fig. 2. Distributed contact states at the PCI, which are significant boundaries for distinguishing wear mechanisms and calculating wear rates, are obtained using a lubrication model. The contact states are fed into a wear calculation model to output the uneven wear contour of the PCI. The uneven wear contour directly affects the geometrical boundaries of the lubrication interface. The uneven wear caused by distributed contact states, in turn, alters the lubrication. The coupling effect between the lubrication and wear contour exists in real-time throughout the operation of APMs. Through this coupling effect, the non-uniform wear distribution at the PCI and its nonlinear evolution process can be predicted.

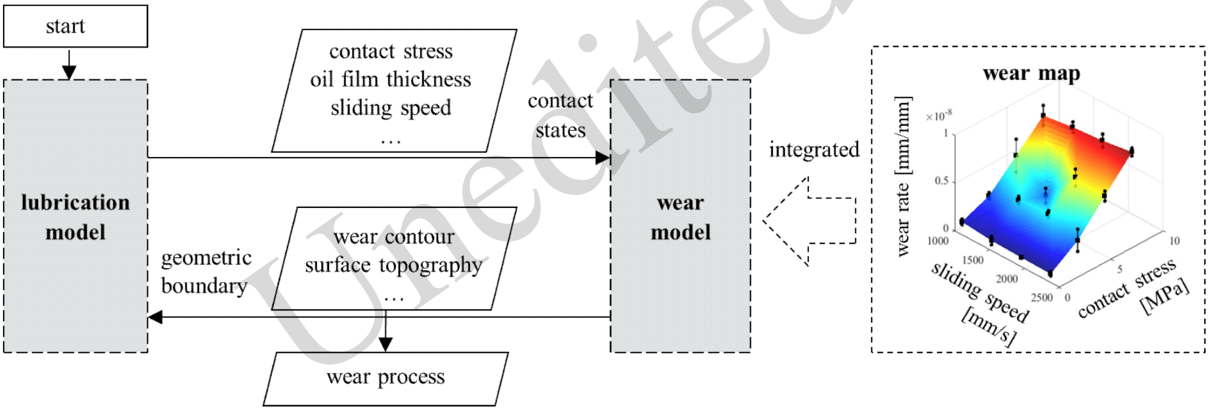

Fig. 2: Brief flowchart of the wear prediction method

The main novelty of the proposed approach lies in replacing existing simplified hard-switching or single wear mechanism models by a wear map to distinguish the combined and complex wear mechanisms and calculate wear rates at the PCI. The distributed contact states, the wear map and its effects are discussed in detail below.

3 Distributed contact states

The contact state, including solid contact stress p_s and sliding speed v_s, directly affects the wear rate of specific contact areas (Aghababaei et al., 2016; Aghababaei and Zhao, 2021; Ghatrehsamani et al., 2021; Khonsari et al., 2021), and consequently could be the key variable of the wear map of the PCI. The contact states in different regions across the entire interface are distinct and constantly change due to the complex and alternating dynamic characteristics of the PCI. A lubrication model that fully accounts for these complex dynamic characteristics was used to characterize the distributed contact state of the PCI, as detailed in Appendix A. The lubrication simulation of the PCI was conducted based on the structural parameters, material parameters and working conditions listed in Table 1.

Table 1. Parameters used in the lubrication model

Parameter	Value
Diameter of piston	8 [mm]
Length of cylinder bore	21.4 [mm]
Angle of swash plate	15 [°]
Yield strength of cylinder bore	280 [MPa]
Elastic modulus of cylinder bore	106 [GPa]
Elastic modulus of piston	206 [GPa]
Poisson's ratio of cylinder bore	0.34 [-]

Poisson's ratio of piston	0.28 [-]
Case drain pressure	0.5 [MPa]
Outlet pressure	28 [MPa]
Rotational speed	5500 [rpm]

To understand the contact states of the PCI, the contact stress distributions in both the high-pressure region (represented at φ=45° and φ=135°) and low-pressure region (represented at φ=225° and φ=315°) are shown in Fig. 3. In Fig. S1 (Appendix A), 0° is defined as the positive X-axis. The circumferential angle θ denotes the rotation from the X-axis toward the Y-axis. z=0 represents the end of the oil film in the axial direction that is near the valve plate, and the opposite end corresponds to the side near the swash plate. The oil film pressure is also presented. In the high-pressure region, the squeezing effect and hydrodynamic effect of the oil film in the PCI gap support the piston well. This keeps the contact stress at the PCI within an acceptable range, which is why APMs are considered components operating on the oil film of lubrication interfaces. However, there is still a certain amount of solid contact stress at the PCI, occurring mainly at the edges of the interface. Note that the oil film pressure and the solid contact stress are solved on a discretized grid (detailed in Appendix B), and the reported values represent grid-averaged quantities within each grid area A_g. Therefore, the oil film pressure peak and contact stress peak discussed here correspond to the maximum grid-averaged values among all grids, which mitigates the non-physical peak near the axial edges that may arise from an idealized sharp-edge geometry.

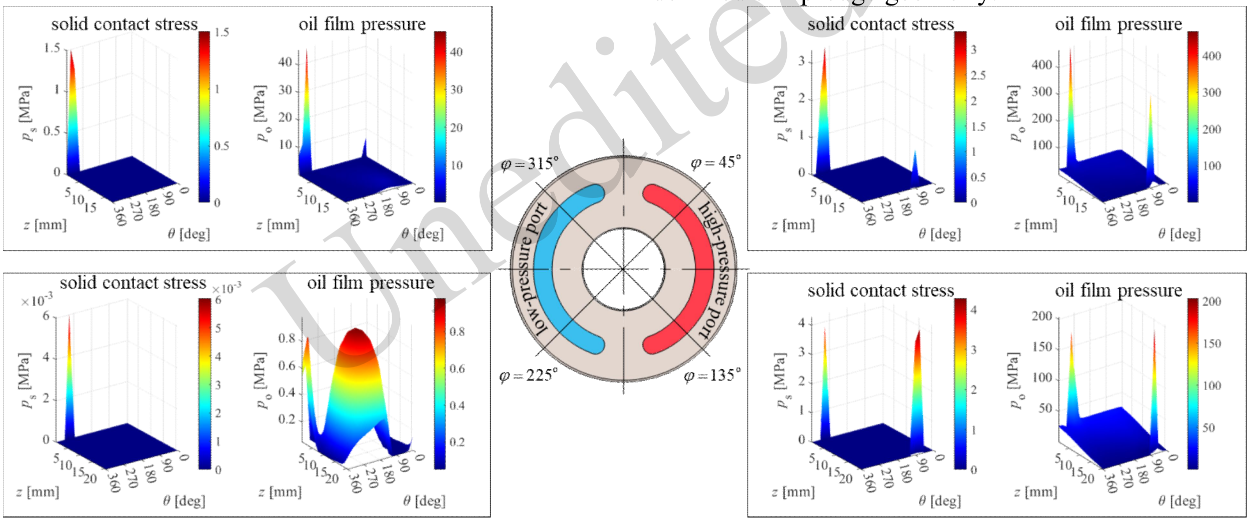

Fig. 3 Contact stress and oil film pressure at different shaft angles

By extracting the peak contact stresses of the PCI at each position, a complete contact stress peak curve at the PCI over one rotation can be obtained. Simultaneously, the resultant sliding speed between the piston and the cylinder bore during one rotation of the cylinder block are calculated (Appendix A). The contact stress peak curve and the sliding speed curve can be combined (Fig. 4(a)) and used to obtain the sliding speed and contact stress matrix required for the disk-on-disk test. Since the contact stress at the PCI is distributed, the contact stress could range from 0 to its peak at any given moment across the entire interface. Various stress levels below the stress peak shown in Fig. 4(a) should be considered, rather than only the peak stress. The range of the contact stress and sliding speed is shown in the blue area in Fig. 4(b), in which each black dot corresponds to the maximum contact stress over the entire PCI and the associated sliding speed at a given shaft angle during one rotation. The blue area represents the operating range of the sliding speed and contact stress used to define the operating condition matrix for the disk-on-disk tests.

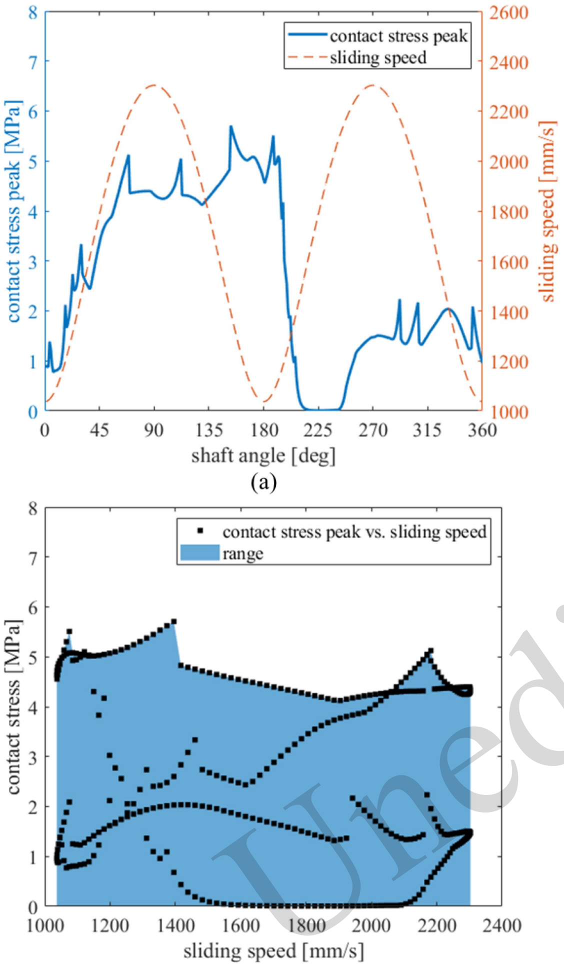

(a)

(b)

Fig. 4 Contact states at the PCI

The range shown in Fig. 4(b) was obtained based on an ideal cylindrical interface. However, as the surface topography changes during the wear process, the contact stress peak correspondingly shifts and is not necessarily monotonically increasing or decreasing (Khonsari et al., 2021). To make the wear map applicable to any wear stage, based on previous research experience (Lyu et al., 2020; Zhang et al., 2021; Lyu et al., 2023), the upper limit of the contact stress range should be higher than the peak in Fig. 4(b). Under practical time constraints, four representative sliding speeds and four representative contact stress levels were selected to provide an evenly distributed coverage of the simulated operating envelope with a manageable number of tests, resulting in the 4×4 matrix listed in Table 2. The upper limit of the contact stress range used to construct the wear map was set one contact stress interval above the maximum value in Fig. 4(b).

Table 2. Operating condition matrix of the wear map

Number	Sliding speed [mm/s]	Contact stress [MPa]
1	2305	8.3
2	2305	5.7
3	2305	3.1
4	2305	0.5
5	1880	8.3
6	1880	5.7
7	1880	3.1
8	1880	0.5
9	1455	8.3
10	1455	5.7
11	1455	3.1
12	1455	0.5
13	1030	8.3
14	1030	5.7
15	1030	3.1
16	1030	0.5

4 Wear map

4.1 Tribometer and specimens

A disk-on-disk tribometer developed by the Institute for Fluid Power Drives and Systems (ifas) at the RWTH Aachen University, Germany, was used to set up the wear map. The disk-on-disk assembly facilitates the direct calculation of contact stress without relying on Hertzian contact theory, and also mitigates the variations in actual contact stress caused by wear. The lower disk was fixed to a drive shaft, while the upper disk was fixed to the static measurement shaft (Fig. 5). A rotating motion was imposed on the lower disk. At the same time, an axial load was applied to the upper disk by a hydraulic cylinder, and the friction torque was measured by a force sensor fixed to the force measurement shaft. The load between the loading component and the force measurement shaft was transmitted through an air bearing, while minimizing the frictional interference between the loading component and the friction force measurement components. The tribometer was equipped with an oil chamber featuring a rotary seal with the driving shaft, enabling specimens to be fully immersed in lubricating oil. A water cooling system around the oil chamber and a temperature sensor were incorporated to prevent overheating during the wear experiments. No.15 aviation hydraulic oil was used in both the tribometer tests and the subsequent APM wear test,. The viscosity of the oil was 15 cSt at 40 °C.

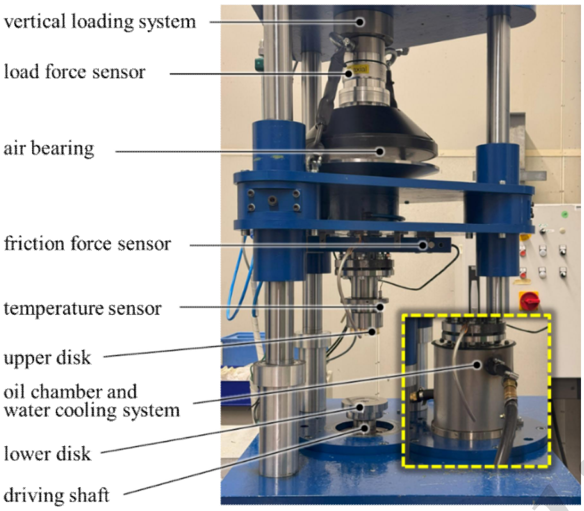

Fig. 5 Disk-on-disk tribometer and its main components

The PCI was composed of a steel piston and a brass cylinder bore to ensure friction compatibility. The brass cylinder bore was softer and undergoes material removal during wear. The fixed upper disk was made of brass (Fig. 5), with its specific chemical composition and mechanical properties detailed in Tables 3 and Table 4. The rotating lower disk was made of alloy steel 38CrMoAl. The average contact area of the disk-on-disk friction pair was 389.56 mm². The original root mean square roughness σ of both samples was 0.15 μm.

Table 3. Chemical composition of the brass friction material [wt.%]

Cu	Zn	Pb	Fe	Mn	Ni	Al	Si	Sn	Other
56.0-59.0	Remaining	0-0.6	0-0.5	2.2-2.8	0-0.5	1.0-2.0	0.5-1.5	0-0.5	0-0.5

Table 4. Mechanical properties of the brass friction material

Yield strength [MPa]	Tensile strength [MPa]	Elongation A5 [%]	Brinell-Hardness [HB 2.5/62.5]
280	590	12	150-185

4.2 Wear assessment

The wear loss can be determined by comparative assessment of the brass disk surface profiles before and after testing. To eliminate the confounding effects of plastic deformation and running-in wear on the profile, dedicated disks were used for each test condition. A standardized procedure consisting of a running-in period was implemented to establish baseline profiles, followed by a subsequent 10-min formal wear test under controlled operating parameters. The procedure is schematically illustrated in Fig. 6(a). The surface roughness was measured after the running-in process and the subsequent 10-min operation, respectively. No measurable change was observed between these two measurements, and the influence of roughness evolution on the wear assessment was excluded.

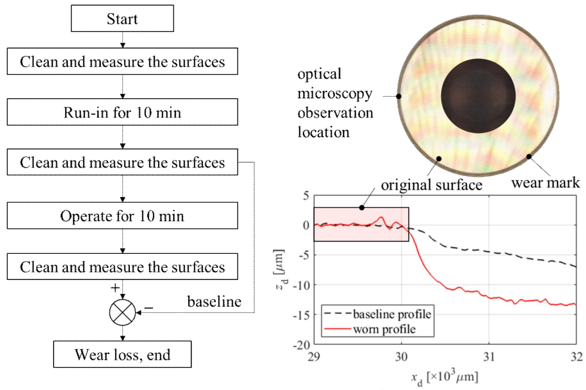

(a) wear map experiment procedure (b) wear assessment

Fig. 6 Procedure of the wear map experiments and wear assessment

The wear profiles were assessed using a Keyence VR-5000 3D profilometer. The wear rates were determined using the volume loss method. Fig. 6(b) shows the wear assessment method. A section of original surface was retained to define the wear depth. Note that edge material tends to accumulate as a result of plastic extrusion, leading to the worn profile at

x_d=29.8 being higher than the baseline profile. The wear volume can be calculated by Eq. (1).

$$V_{\mathrm{w}} = \int_{R_0}^{R_{\mathrm{d}}} \left(2\pi \cdot x_{\mathrm{d}} \cdot \left|z_{\mathrm{d}}\right|\right) \mathrm{d}x_{\mathrm{d}} , \qquad (1)$$

where R_d is the outer radius of the disk (32 mm), R_0 is the distance from the starting point of the measurement to the disk center, x_d is the distance from the measurement point to the disk center, and z_d is the wear depth of the measurement point. The location of optical microscopy observation on the specimen is also indicated in Fig. 6(b).

In the lubrication model, the wear distribution is represented on the geometric boundary as depth variations at each node. Therefore, the wear depth per unit sliding distance, i.e., the linear wear rate (Wen and Huang, 2017), should be calculated from Eq. (2):

$$w_{\mathrm{h}} = \frac{V_{\mathrm{w}}}{A_{\mathrm{c}}} , \qquad (2)$$

where A_c is the average contact area of the disk-on-disk friction pair.

4.3 Wear map characterization

The measured wear map is presented in Fig. 7(a), illustrating variation in the wear rate under different contact stresses and sliding speeds. Due to the minimum load limitation of the tribometer, linear extrapolation was applied in the region below 0.5 MPa. In the low contact stress regime, the wear rate was small and within the operating range considered in this study, and the extrapolation was expected to have a limited effect on the accumulated wear prediction. Nevertheless, the wear map accuracy in the untested regime below 0.5 MPa remained uncertain. Each operating condition in Table 2 was tested three times. The mean wear rate of the three repeats was used to construct the wear map in Fig. 7, in which the corresponding scatter is indicated by error bars. The measured wear rate increased nonlinearly with contact stress, rising slowly under low contact stress conditions and then more rapidly over the stress within the operating range considered. The wear rates showed no clear monotonic trend with sliding speed. However, the wear rate at 5.7 MPa exhibited a more pronounced variation with sliding speed than the wear rate at the other stress levels (Fig. 7(b). Notably, the wear rate at 5.7 MPa and a sliding speed of 1455 mm/s exhibited a reduction relative to the adjacent conditions. Although a definitive physical explanation is not yet available, the repeated tests gave similar results under this operating condition. Therefore, this data point was retained and used in the present analysis.

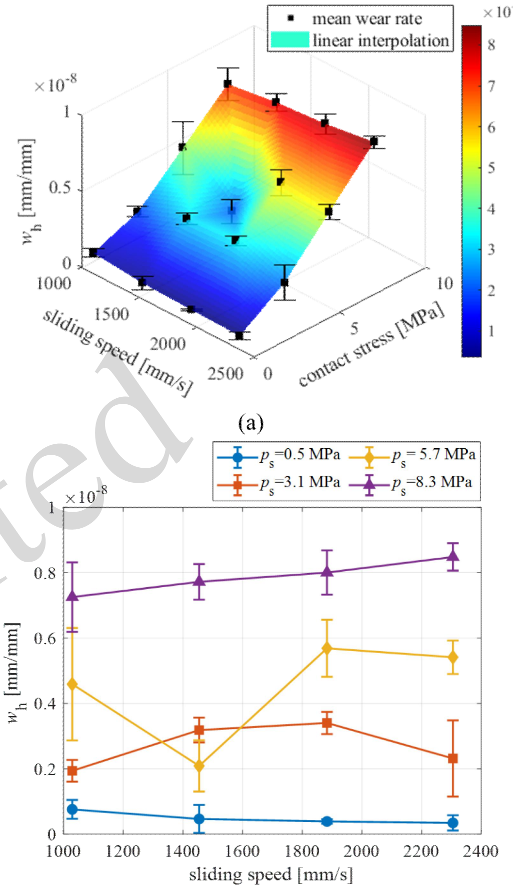

(a)

(b)

Fig. 7 Wear map representation

Fig. 8 presents representative optical micrographs obtained using an Alicona Infinite Focus 3D optical profilometer at 50× magnification under different contact stresses and sliding speeds. At the lowest contact stress (0.5 MPa), the surface was dominated by ploughing scratches aligned with the sliding direction. With increasing contact stress (3.1 MPa), a smoother and more polished surface appearance was observed. At the intermediate stress (5.7 MPa), polishing remained evident while local adhesive marks appeared. At the highest stress (8.3 MPa), adhesive marks and material transfer became more pronounced.

These observations indicate a transition in wear features with increasing contact stress, from scratch-dominated abrasion/polishing toward more adhesive-dominated behavior within the investigated envelope. At intermediate stress levels, the coexistence of polishing and local adhesive marks suggests a mixed-mechanism regime, which may be more sensitive to sliding speed. This provides a plausible interpretation for the more pronounced speed-dependent fluctuation observed at 5.7 MPa. Nevertheless, a definitive mechanism for the local reduction at 1455 mm/s was not established in this present study. It is an observation that warrants further targeted investigation into the underlying mechanism.

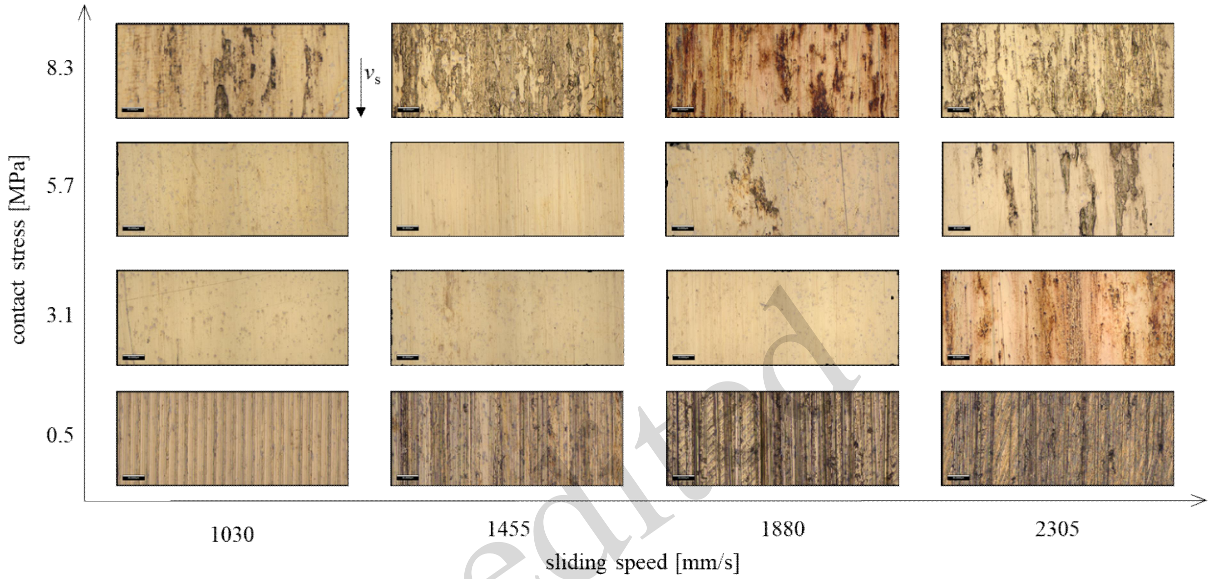

Fig. 8 Optical micrographs at different sliding speeds and contact stresses

The optical micrographs revealed the coexistence of combined and complex wear mechanisms across the entire PCI, fundamentally challenging the existing oversimplified single mechanism assumptions. To further confirm the necessity of this wear map, the differences between the existing single mechanism wear model and the proposed wear map were quantitatively elaborated. Most previous studies on the wear processes of frictional interfaces (Brinkschulte et al., 2018; Ivantysyn et al., 2020; Lin et al., 2024) assumed adhesion to be the predominant wear mechanism. The Archard model , the most widely used model for adhesive wear, is used for single mechanism wear rate calculation (Archard, 1953). The linear wear rate w_a derived from the Archard model is calculated by Eq. (3):

$$w_a = k_a \frac{p_s}{3\sigma_s}, \tag{3}$$

where k_a is the Archard wear coefficient and σ_s is the yield strength of the cylinder bore material.

To compare the measured wear map with the conventional single mechanism Archard model, the predicted wear rate distribution over the operating range shown in Fig. 4 was plotted (Fig. 9). Previous experimental studies indicated that under a consistent lubrication condition, the adhesive wear coefficient remains constant when surface contact stress does not exceed one third of the yield strength of the material (Burwell and Strang, 1952). The contact stress peak at the PCI was far below this threshold according to the calculation in Section 3.2 and the mechanical properties in Table 4, so that the adhesive wear coefficient theoretically remained constant in the conventional Archard model. Under this assumption, the assumed Archard wear coefficient k_a in Eq. (3) was estimated by linear regression of the measured wear rates in Fig. 7(a), as expressed in Eq. (4):

$$k_a = \frac{\sum_{i=1}^{N} \left(p_i / \sigma_s \right) w_{hi}}{\sum_{i=1}^{N} \left(p_i / \sigma_s \right)^2}, \tag{4}$$

where N is the total number of tribometer operating conditions, i is the index of an operating condition, p_i is the contact stress at the i^{th} condition, and w_{hi} is the measured linear wear rate at the i^{th} condition.

The Archard wear model predicts a wear rate that is independent of sliding speed and increases linearly with contact stress. Although the measured wear map also exhibited a general increase in wear rate with contact stress and only a minor dependence on sliding speed, the trend was not strictly linear as in the Archard model (Fig. 9). Instead, due to transitions in wear mechanisms, the overall wear rate first increased slowly and then more rapidly with increasing contact stress. Moreover, at intermediate stress levels, where multiple wear mechanisms coexist, the wear rate varied noticeably with sliding speed, which further distinguishes the measured wear behavior from the Archard model.

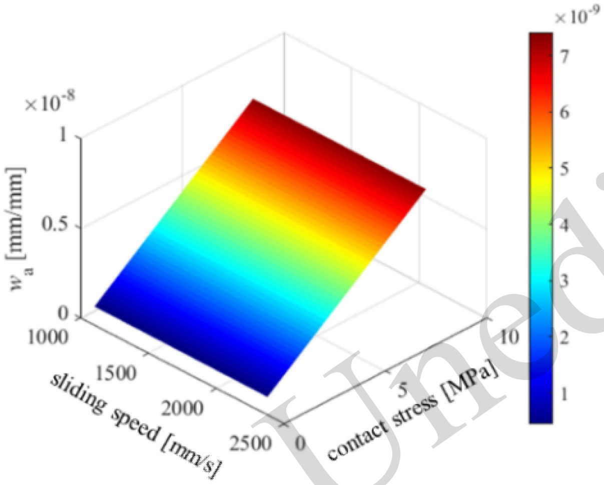

Fig. 9 Wear map derived from Archard model

Compared with the conventional Archard model, the measured wear map provides a more flexible mapping from contact stress and sliding speed to wear rate over the operating envelope of the PCI. Within the scope and resolution of the current dataset, both approaches capture the dominant influence of contact stress, while the wear map was adopted in the wear prediction to incorporate the observed non-strictly linear dependence on contact stress and the possible interaction between sliding speed and contact stress at intermediate stress levels.

Several limitations should be noted. The measured wear map was established from the disk-on-disk tribometer tests under the configuration and protocol described in Section 4.1. The resolution of the wear map was limited by the operating condition matrix used in the present dataset. The sensitivity to tribometer parameters has not been systematically quantified. These parameters include surface preparation, alignment, oil supply condition, bulk oil temperature control, and the running-in protocol. In addition, the measured wear map was obtained for the specific lubricant/material pairing used in this study (No.15 aviation hydraulic oil and the steel piston against the brass cylinder bore). Transferability to other pump sizes, material pairs, and lubricants has not been validated. Recalibration is expected to be needed when substantial changes are introduced. Finally, fresh oil was used in the present tests. Oil aging and contaminant particles were not considered. Therefore, the measured wear map is conditional on the adopted test procedure and oil condition.

4.4 Integration of the wear map with wear prediction method

This section discusses the methodology for integrating wear maps into wear prediction models and delineates their scope of application. Under ideal conditions, once the contact stresses and sliding speeds at each node of the oil film are determined by the lubrication model, the corresponding wear rate at each node can be interpolated from the wear map. Subsequently, the wear depth h_w at each node per time step is calculated. This process is expressed mathematically as:

$$h_{\mathrm{w}}(\theta,z)=\omega_{\mathrm{h}}\left(p_{\mathrm{s}}(\theta,z),v_{\mathrm{s}}(\theta,z)\right)\Delta s\,, \tag{5}$$

where Δs is the incremental sliding distance between the piston and bore per time step.

This disk-on-disk friction pair needs to operate predominantly under boundary lubrication, thereby minimizing elastohydrodynamic lubrication (EHL) effects that could reduce actual contact stresses below theoretical predictions. Due to limitations of the test conditions, the lubrication regime was inferred from the friction coefficient rather than from direct measurements of the oil film thickness. During the tribometer test, the friction coefficients under all operating conditions ranged from 0.11 to 0.24. The disk-on-disk wear test maintained stable operation in the boundary lubrication regime in which the friction coefficients typically exceed 0.1. According to classical lubrication theory, the film thickness ratio λ shown in Eq. (6) is conventionally defined as being less than 1 when characterizing boundary lubrication (Zhu and Wang, 2012; Wen and Huang, 2017). Consequently, when applying wear maps to PCI wear calculations, a critical constraint of $\lambda \leq 1$ must be imposed.

$$\lambda = \frac{h_{\mathrm{o}}}{\sigma}. \tag{6}$$

where h_{o} is the oil film thickness and σ is the RMS roughness, as detailed in Appendix A.

5 Effects of the wear map on wear prediction

By integrating the experimentally measured wear map into the wear prediction model following the workflow outlined in Fig. 2, the temporal evolution of the wear contour of the cylinder bore can be numerically simulated. To evaluate the effectiveness of our proposed method, simulation results from the wear map-based method were compared with those from the widely used Archard model-based method (Brinkschulte et al., 2018; Zhang et al., 2021; Lin et al., 2024). An APM wear test was conducted to validate the results.

5.1 APM wear test setup

The APM wear test consisted mainly of an operating procedure and surface measurement. The process of the APM wear test is shown in Fig. 10. To track the wear evolution process, the test started with the surface measurement of a new APM. Then, after operating for a specified period, the APM was disassembled to measure the wear contour of the PCI during this period. The process was repeated, and the wear contours after operating for 0.5, 3, 9 and 15 h were measured. Due to limitations of the test resources, the pump wear validation was conducted on only a single APM. Therefore, variability between multiple pump tests was not quantified in the present study. The details of the test and measurement are shown in Appendix C.

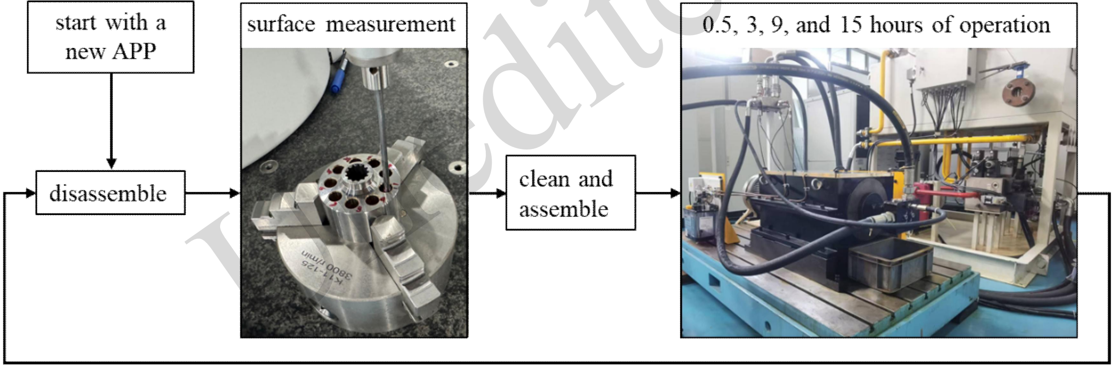

Fig. 10 Process of the APM wear test

5.2 Comparison of results

The experimental results from the two simulation methods were compared. In the wear prediction simulation, the maximum wear depth of a single revolution of the cylinder bore was below 10^{-2} μm, which is too small to influence the lubrication state. Therefore, after each geometric boundary update, the wear increment was linearly accumulated until the maximum wear depth exceeded a threshold (Lyu et al., 2020). At each update, the accumulated wear depth field h_{w} was applied to update the local film-thickness distribution and the geometric boundary of the lubrication model, and the mixed lubrication model was re-run based on the updated geometry to obtain the updated lubrication/contact state for the subsequent wear accumulation. Consequently, the geometric boundaries and the lubrication boundaries were not continuously updated over time. However, the update time points in the simulation that were closest to the experimental time points can still be used to compare the results. According to the operation time in Fig. 10, four comparison time points t_1 to t_4 were defined, and the corresponding simulation time points are shown in Table 5. We acknowledge that the PCI was initialized using an ideal cylindrical geometry, and manufacturing tolerances or as-built geometric deviations were not explicitly considered here.

Table 5 Comparison of experimental and simulation times at the defined time points

Defined comparison time point	Experimental time [h]	Simulation time of wear map-based wear prediction	Simulation time of Archard model-based wear

		method [h]	prediction method [h]
t_1	0.50	0.64	0.54
t_2	3.00	3.26	3.05
t_3	9.00	9.51	9.66
t_4	15.00	17.27	15.99

The wear contours obtained by the wear test and the two wear prediction methods at the four time points are shown in Fig. 11, which reveals not only the wear distribution, but also the evolution process of the wear distribution over time. The wear regions were mainly at the two ends of the cylinder bore. For clarity, the end of $z = 0$ was defined as the bottom end, and the opposite end as the top end.

The experimental results and the simulation results from the two wear prediction models showed consistency in several aspects. At the top end, significant wear appeared early in the circumferential range of 135° to 225° at t_1. Then at t_2, wear began to develop at around 335° at the bottom end and increased rapidly from t_2 to t_4. Meanwhile, the wear evolution was less pronounced at the top end than at the bottom end.

Although both the wear map-based method and the Archard model-based method can predict the regions where wear appears, the Archard model-based method significantly underestimated the wear at the bottom end compared with the wear map-based method. Both methods predicted the increase of the wear at the bottom end from t_2 to t_4, but the Archard model-based method predicted a slower rate of increase than the wear map-based method.

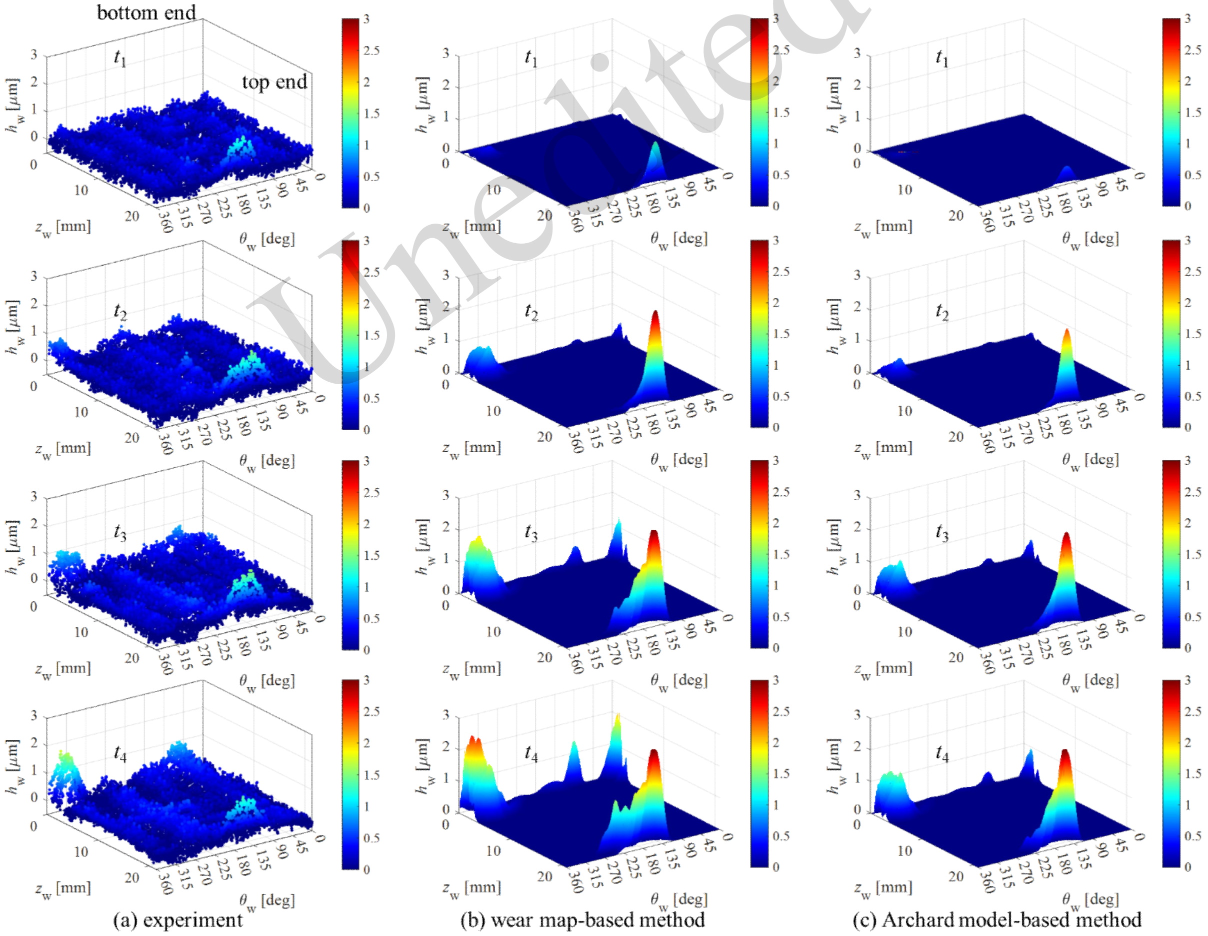

(a) experiment (b) wear map-based method (c) Archard model-based method

Fig. 11 Evolution of the PCI wear contour predicted by different approaches

To quantify the differences in predicting wear characteristics at the top and bottom of the cylinder bore between the wear map-based method and the Archard model-based method, the wear volume at the top of the cylinder bore, V_{wt}, and the wear volume at the bottom of the cylinder bore, V_{wb}, were calculated. The calculation method was:

$$V_{\mathrm{wb}}^{t}=\int_{0}^{\frac{L_{\mathrm{c}}}{2}}\int_{0}^{360}\left[h_{\mathrm{w}}^{t}\left(\theta,z\right)-h_{\mathrm{w}}^{0}\left(\theta,z\right)\right]\mathrm{d}z\mathrm{d}\theta\,, \quad (7)$$

$$V_{\mathrm{wt}}^{t}=\int_{\frac{L_{\mathrm{c}}}{2}}^{L_{\mathrm{c}}}\int_{0}^{360}\left[h_{\mathrm{w}}^{t}\left(l,\theta\right)-h_{\mathrm{w}}^{0}\left(l,\theta\right)\right]\mathrm{d}z\mathrm{d}\theta\,, \quad (8)$$

where L_c is the length of the cylinder bore. The upper index t is the time point, in which 0 represents the original time point. The quantitative evolution obtained by the wear test and the two wear prediction methods at the four time points are shown in Fig. 12. The experimental results in Fig. 12(a) show that V_{wt} increased rapidly at the early stage, whereas V_{wb} exhibited a more pronounced growth in the later stage, and approached and even surpassed V_{wt}. This indicates a progressive redistribution of wear dominance from the top end to the bottom end during the test. When faster wear is accumulated at one end, a larger local clearance can be produced. A lower local contact stress can then be obtained, and a saturation-like behavior can be developed. A progressive shift of wear activity toward the opposite end can then be promoted. This mechanism is consistent with the observed trends of V_{wt} and V_{wb}. The physical cause was not determined in the present study. Therefore, the redistribution is reported as an experimental observation.

The results predicted by the wear map-based method are shown in Fig. 12(b). The wear map-based method reproduced this redistribution more consistently: it predicted a faster increase of V_{wb} in the later stage and captured the crossover trend ($V_{\mathrm{wb}} > V_{\mathrm{wt}}$) observed in the measurements. The predicted end-region wear volumes at the final time point also showed closer agreement with the experimental values.

In contrast, the Archard model-based method in Fig. 12(c) yielded a nearly proportional growth of wear volume with time and predicted that V_{wt} would remain slightly higher than V_{wb} at the final time point, which did not reproduce the experimentally observed crossover. In addition, the Archard predictions underestimated the end-region wear volumes, with the deviation being more pronounced at the bottom end.

Overall, both methods could identify the end-wear regions. However, the quantified evolution of V_{wt} and V_{wb} indicates that the wear map-based method captures the temporal redistribution between the two ends more consistently, whereas the Archard model-based method does not reproduce the crossover behavior observed in the measurements.

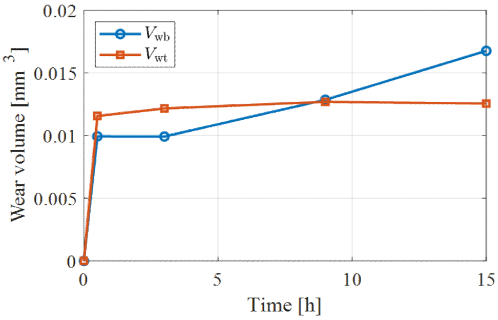

(a) experiment

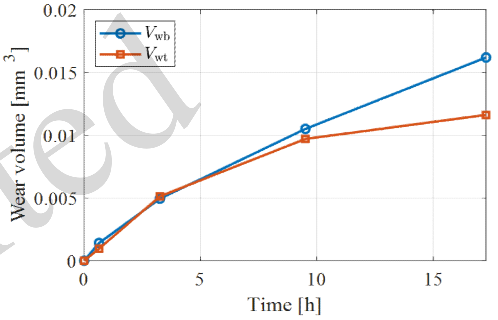

(b) wear map-based method

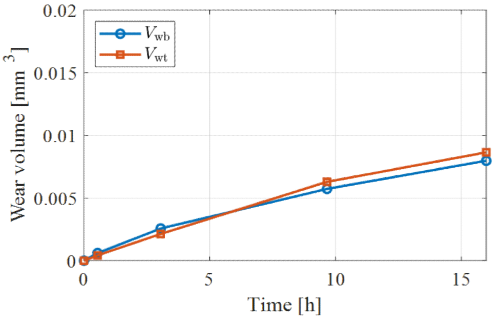

(c) Archard model-based method

Fig. 12 Quantitative evolution of the wear volume at top end and bottom end

6 Conclusions and outlook

In this paper, a wear map-based wear prediction method is proposed. The fundamental principle involves embedding a wear map representing the wear rate over the entire contact state of the PCI into an existing wear prediction framework as the wear calculation sub-model. The main conclusions are as follows:

1. Disk-on-disk tribometer results showed that

the wear rate increased nonlinearly with contact stress, and the sensitivity to sliding speed became more noticeable at intermediate stress levels within the investigated operating envelope.

2. Pump wear tests showed that wear appears mainly at both axial ends of the cylinder bore. Both the wear map-based method and the conventional Archard model-based method were able to identify the main wear regions at the PCI.

3. Regarding the wear evolution process, at the top end, wear appeared early, within 0.5 h, and then grew more slowly. At the bottom end, wear increased rapidly from 3 h, and by 15 h reached a level higher than that at the top end. The conventional Archard model-based method underestimated the wear increment at the bottom end and did not reproduce the experimentally observed wear volume crossover between the two ends at the final time point. The wear map-based method captured this redistribution more consistently.

The wear map-based method has the capability to predict the wear behavior of frictional interfaces with multiple coexisting contact states such as a PCI. Targeted engineering implications can be drawn. Candidate material pairing and surface condition for the PCI in APMs can be screened by initial disk-on-disk tribometer tests combined with wear prediction, without the immediate need for APM prototyping. For existing APMs, a more targeted and physics-consistent wear prediction can be provided to support predictive maintenance. A physics-informed neural network prediction model can be explored in the future to improve prediction accuracy.

Nevertheless, time-consuming dedicated measurements are required. The present wear map was measured for a specific lubricant/material pairing, and transferability to other lubricants and material pairs was not validated. Therefore, future work will focus on wear mechanisms and metal-oil interaction by microscale and mechanism-oriented methods, for example molecular dynamics, to support the calculation and generalization of the wear map.

Acknowledgments

This work is supported by the National Natural Science Foundation of China (No. 52305075 and No. U24B2049), the Fundamental Research Funds for the Zhejiang Provincial Universities (No. 226-2025-00204), and the China Postdoctoral Science Foundation (No. 2023M733065).

Author contributions

Fei LYU: Conceptualization, Methodology, Writing-original draft. **Xudong SHEN**: Validation, Data curation. **Felix SCHLEGEL**: Investigation, Writing-review & editing. **Xiaolong ZHANG**: Project administration. **Liangyu SONG**: Visualization. **Junhui ZHANG**: Software, Funding acquisition. **Katharina SCHMITZ**: Resources, Supervision. **Bing XU**: Resources, Supervision.

Conflict of interest

Fei LYU, Xudong SHEN, Felix SCHLEGEL, Xiaolong ZHANG, Liangyu SONG, Junhui ZHANG, Katharina SCHMITZ and Bing XU declare that they have no conflict of interest.

Data availability

The data that support the findings of this study are available from the corresponding author upon reasonable request.

References

Aghababaei R, Warner DH, Molinari J-F, 2016. Critical length scale controls adhesive wear mechanisms. *Nature Communications*, 7(1):1-8.

Aghababaei R, Zhao K, 2021. Micromechanics of material detachment during adhesive wear: A numerical assessment of Archard's wear model. *Wear*, 476:203739.

Archard J, 1953. Elastic deformation and the contact of surfaces. *Nature*, 172(4385):918-919.

Brinkschulte L, Mattes J, Geimer M, 2018. An approach to wear simulation of hydrostatic drives to improve the availability of mobile machines. 11th International Fluid Power Conference.

Burwell JT, Strang CD, 1952. On the Empirical Law of Adhesive Wear. *Journal of Applied Physics*, 23(1):18-28.

Ernst M, Vacca A, 2021. Hydrostatic vs. hydrodynamic components of fluid pressure in the tribological interfaces of axial piston machines. *Tribology International*, 157:106878.

Fleischer G, 1973. Energetische methode der bestimmung des verschleißes. *Schmierungstechnik*, 4(9):269-274.

Gärtner M, Holzer A, Fischer F, et al., 2019. EHL Simulation model for an abstracted piston-bushing test Rig. *Tribologie und Schmierungstechnik*, 66(6):9-16.

Ghatrehsamani S, Akbarzadeh S, Khonsari M, 2021. Experimental and numerical study of the running-in wear coefficient during dry sliding contact. *Surface Topography: Metrology and Properties*, 9(1):015009.

Gong T, Yao P, Xiao Y, et al., 2015. Wear map for a copper-based friction clutch material under oil lubrication. *Wear*, 328:270-276.

Guo L, Zhu W, Shi L, et al., 2019. Study on wear transition mechanism and wear map of CL60 wheel material under dry and wet conditions. *Wear*, 426:1771-1780.

Ivantysyn R, Shorbagy A, Weber J, 2020. Investigation of the wear behavior of the slipper in an axial piston pump by means of simulation and measurement. 12th International Fluid Power Conference.

Khonsari M, Ghatrehsamani S, Akbarzadeh S, 2021. On the running-in nature of metallic tribo-components: A review. *Wear*, 474-475:203871.

Kumar S, 2024. Comprehensive Review on Role of Surface Modification Techniques to Prevent Failure of IC Engine Parts. *Protection of Metals and Physical Chemistry of Surfaces*, 60(2):218-269.

Lin Y, Wang H, Wang H, et al., 2024. A novel wear prediction method and wear characteristic analysis of piston/cylinder pair in axial piston pump. *Wear*, 550:205402.

Lyu F, Zhang J, Sun G, et al., 2020. Research on wear prediction of piston/cylinder pair in axial piston pumps. *Wear*, 456:203338.

Lyu F, Zhang J, Zhao S, et al., 2023. Coupled evolution of piston asperity and cylinder bore contour of piston/cylinder pair in axial piston pump. *Chinese Journal of Aeronautics*, 36(8):395-407.

Mattei L, Di Puccio F, Ciulli E, et al., 2020. Experimental investigation on wear map evolution of ceramic-on-UHMWPE hip prosthesis. *Tribology International*, 143:106068.

Patir N, Cheng H, 1978. An average flow model for determining effects of three-dimensional roughness on partial hydrodynamic lubrication. *Journal of Tribology*, 100(1):12-17.

Ransegnola T, Shang L, Vacca A, 2022. A study of piston and slipper spin in swashplate type axial piston machines. *Tribology International*, 167:107420.

Schenk A, 2014. Predicting lubrication performance between the slipper and swashplate in axial piston hydraulic machines. PhD Thesis, Purdue University, West Lafayette, USA.

Vásquez-Chacón IA, Gómez-Guarneros MA, Sanchez-Tizapantzi P, et al., 2022. A pin-on-disk wear map of rail and wheel materials from different standards. *Materials Letters*, 307:131021.

Wang W, Chao Q, Shi J, et al., 2025. Condition monitoring of axial piston pumps based on machine learning-driven real-time CFD simulation. *Engineering Applications of Computational Fluid Mechanics*, 19(1):2474676.

Wen S, Huang P, 2017. Principles of tribology. *John Wiley & Sons*, Hoboken, USA, p.1-21.

Wondergem AM, Ivantysynova M, 2015. The impact of micro-surface shaping on the piston/cylinder interface of swash plate type machines. ASME/BATH 2015 Symposium on Fluid Power and Motion Control.

Xia S, Xia Y, Xiang J, 2022. Piston wear detection and feature selection based on vibration signals using the improved spare support vector machine for axial piston pumps. *Materials*, 15(23):8504.

Xu B, Zhang J, Yang H, et al., 2013. Investigation on the radial micro-motion about piston of axial piston pump. *Chinese Journal of Mechanical Engineering*, 26(2):325-333.

Yin F, Chen Y, Ma Z, et al., 2023. Investigation on mixed thermalelstohydrodynamic lubrication behavior of slipper/swash plate interface in water hydraulic axial piston pump. *Tribology International*, 189:108896.

Zhang C, Zang Y, Wang H, et al., 2023. Theoretical and experimental investigation on the efficiency of a novel roller piston pump. *Journal of Zhejiang University-SCIENCE A*, 24(9):762-781.

Zhang J, Lyu F, Xu B, et al., 2021. Simulation and Experimental Investigation on Low Wear Rate Surface Contour of Piston/Cylinder Pair in an Axial Piston Pump. *Tribology International*, 162:107127.

Zhang J, Shen Y, Lyu F, et al., 2024. Tolerance design guideline for piston/cylinder interface of electro-hydrostatic actuator (EHA) pumps based on a thermal-fluid-structure model. *Tribology International*, 191:109208.

Zhang X, Zhang K, Kang X, et al., 2021. Friction maps and wear maps of Ag/MoS2/WS2 nanocomposite with different sliding speed and normal force. *Tribology International*, 164:107228.

Zhu D, Wang QJ, 2012. On the λ ratio range of mixed lubrication. *Proceedings of the Institution of Mechanical Engineers, Part J: Journal of Engineering Tribology*, 226(12):1010-1022.

Electronic supplementary materials

Appendix A, Appendix B, Appendix C

中文概要

题　目：基于磨损图的轴向柱塞泵/马达柱塞副磨损预测方法

作　者： 吕飞[1,2]，沈旭栋[1]，Felix SCHLEGEL[2]，张小龙[1]，宋良宇[1]，张军辉[1]，Katharina SCHMITZ[2]，徐兵[1]

机　构： [1]浙江大学，流体动力基础件与机电系统全国重点实验室，中国杭州，310058；[2]亚琛工业大学，流体驱动与系统研究所，德国亚琛，52074

目　的： 预测柱塞副的磨损行为对于提高轴向柱塞泵/马达的可靠性和服役寿命至关重要。本文旨在通过柱塞副磨损图来改进现有磨损进程预测模型中通过摩擦副润滑状态硬切换单/双磨损模型计算磨损率不准确的问题，实现更加全面和准确的柱塞副磨损进程预测。

创新点： 本文主要新颖之处在于提出了基于实测磨损图的磨损预测方法，替代现有的简化硬切换磨损计算

模型，获得柱塞副复合磨损机制下，界面全域接触状态与磨损率的映射关系。

方　法：1. 使用柱塞副混合润滑模型描述了摩擦副界面全域接触状态，并将其作为工况矩阵输入盘-盘摩擦磨损试验台，获得柱塞副全域接触状态磨损图，建立接触状态与磨损率的映射关系。2. 通过观测柱塞副全域接触状态下磨损特征的复合性，阐明磨损图的必要性。3. 将磨损图嵌入到柱塞副磨损进程预测模型中分析磨损图对磨损分布和演化进程的影响，并通过整泵磨损进行验证。

结　论：1. 柱塞副局部磨损率随接触应力非线性增加，并且在所研究的接触工况内的中间应力水平下，对滑动速度的敏感性较明显。2. 从磨损轮廓来看，磨损主要出现在缸孔轴向两端，基于磨损图的方法和传统的基于 Archard 模型的方法都能够识别主要磨损区域。3. 从磨损演化进程来看，0.5 小时内缸孔顶端迅速出现磨损，然后顶端磨损增长缓慢。在缸孔底端，磨损从 3 小时起迅速增加，到 15 小时达到比顶端更高的水平。传统的基于 Archard 模型的方法未重现底端磨损量的反超，基于磨损图的方法更一致地捕获了这种缸孔两端磨损量随着时间的重新分布情况。

关键词：磨损图；磨损演化；混合润滑；柱塞副；轴向柱塞泵/马达